catalysts

MDPI

Article

A Scalable One-Pot Synthesis of a Durable Iridium Nanocatalyst for High-Performance PEM Water Electrolysis

Chuan Long [1,†], Yi An [1,2,†], Bowen Xia [1], Feifei Fang [1], Jingjing Wang [1], Chenyi Shao [1], Yinglong Yu [1,*], Haicheng Xiao [1,*] and Yanfei Wang [1,*]

[1] Petrochina Petrochemical Research Institute, Beijing 102206, China
[2] School of Chemistry and Materials Science, University of Science and Technology of China, Hefei 230026, China
* Correspondence: yuyinglong@petrochina.com.cn (Y.Y.); xhc459@petrochina.com.cn (H.X.); wangyanfei010@petrochina.com.cn (Y.W.)
† These authors contributed equally to this work.

Abstract

Proton exchange membrane water electrolysis (PEMWE) is currently limited by the sluggish kinetics and poor durability of the oxygen evolution reaction (OER). In this work, a structurally uniform $IrB_{160\text{-}4}$ catalyst was synthesized through a simple, scalable one-pot aqueous method. This template-free method enables near-quantitative yields and gram-scale preparation, with products rapidly separated via simple filtration. The catalyst consists of uniform, nanoclusters self-assembled from highly crystalline ~3 nm Ir nanoparticles. The optimized catalyst exhibits superior OER activity over commercial Ir-Black. The assembled proton exchange membrane electrolyzer, utilizing a low anodic iridium loading of 0.5 mg cm^{-2}, demonstrates excellent performance (2.0 A cm^{-2} @ 1.79 V) and high durability (>1500 h). This synthesis strategy provides a feasible method for achieving efficient and stable PEM water electrolysis for hydrogen production.

Keywords: PEM water electrolysis; electrocatalysis; Iridium catalyst; oxygen evolution reaction; durability

1. Introduction

Producing green hydrogen through water electrolysis powered by clean and renewable energy sources is widely regarded as a promising pathway to alleviate the global energy crisis and facilitate the achievement of carbon neutrality [1–4]. Among various electrolysis technologies, proton exchange membrane water electrolysis (PEMWE) exhibits several compelling advantages, including high current density, excellent energy efficiency, rapid dynamic response, and the production of ultrahigh-purity hydrogen [5,6]. Benefiting from these advantages, PEMWE is widely considered the most compatible water-electrolysis technology for integration with fluctuating renewable energy sources [7,8]. However, the large-scale commercialization of PEMWE is still hindered by the lack of high-performance and cost-efficient electrocatalysts. This is primarily because the overall efficiency of PEMWE is severely restricted by the sluggish kinetics of the anodic OER [7,9–13]. To improve the efficiency of PEMWE systems, various anodic OER catalysts have been designed and explored [14–21]. However, most of these catalysts still suffer from insufficient durability under the harsh operating conditions of PEMWE, where strongly acidic media and high anodic potentials accelerate metal dissolution, structural collapse, and loss of active sites [22–28]. These degradation processes ultimately hinder long-term stable operation

Academic Editor: David Sebastián

Received: 19 March 2026
Revised: 29 April 2026
Accepted: 1 May 2026
Published: 6 May 2026

and significantly limit practical application. In particular, Iridium-based catalysts remain among the few OER materials that can simultaneously offer high activity and sufficient stability under industrial PEMWE operating conditions, making them the most widely adopted choice to date [29,30].

To enhance the catalytic activity and precious metal utilization of Ir-based catalysts, significant research efforts have been dedicated to nanostructuring, leading to the development of various nano-catalysts, including nanowires, hollow spheres, and core–shell structures [31–37]. However, these strategies, while pursuing high activity, also present severe challenges. On the one hand, these nanostructures possess high specific surface areas and high surface energies, making them susceptible to electrochemical dissolution and agglomeration under the harsh operating potentials of the OER. This leads to rapid catalyst deactivation, structural collapse, and ultimately, compromised long-term stability. On the other hand, the fabrication of these catalysts often relies on complex, multi-step synthetic routes, template-assisted methods, or pathways involving large quantities of organic solvents. This not only hinders scalable production but also raises significant environmental concerns. For practical applications, long-term durability and synthetic simplicity are often as critical as, if not more important than, maximizing the initial activity. Therefore, there is an urgent need to develop an Ir-based OER catalyst that combines a simple synthesis, controllable morphology, high activity, and high durability.

Herein, we report a structurally uniform Ir nanocatalyst synthesized via a simple, template-free, one-pot aqueous-phase method. This synthesis method avoids the use of organic solvents and tedious purification steps, and the product can be rapidly isolated by simple filtration, demonstrating potential for scale-up production. In contrast to conventional methods, which typically yield nanoparticles prone to uncontrolled agglomeration and lacking long-range structural order, the as-prepared catalyst (named $IrB_{160\text{-}4}$) exhibits exceptional structural uniformity. It consists of highly crystalline ~3 nm Ir nanoparticles that self-assembled into uniform nanospheres (~50 nm), maintaining high uniformity even at the micrometer scale. This morphology contributes to enhanced activity and stability of the catalyst. $IrB_{160\text{-}4}$ shows higher activity and stability than commercial Ir-Black. In membrane electrode assembly (MEA) testing, $IrB_{160\text{-}4}$ achieved a high current density of 2 A cm^{-2} at 1.79 V and demonstrated excellent operational stability for over 1500 h.

2. Results and Discussion

2.1. Synthesis Strategy and Formation Mechanism

The catalyst was synthesized via a facile one-pot aqueous method, as illustrated in Figure 1a Initially, chloroiridic acid and citric acid were thoroughly mixed in an aqueous solution. Subsequently, KOH was introduced, serving a dual crucial role: (i) It deprotonates the citric acid to form citrate ions (Cit^{3-}), which act as strong chelating ligands for the $[IrCl_6]^{2-}$ precursor. This strong chelation is essential for stabilizing the Ir precursor, preventing its premature precipitation or hydrolysis. (ii) It provides an alkaline reaction medium, establishing the necessary chemical environment for the subsequent reduction process. Next, a strong reducing agent, $NaBH_4$, was introduced into the system. The alkaline environment is critical for modulating the reduction kinetics of $NaBH_4$, thereby promoting the uniform and controlled nucleation of ultrasmall Ir(0) nanoparticles. At this stage, the nanoparticles are stabilized by a surface-adsorbed citrate layer, which effectively inhibits immediate particle aggregation. Finally, the colloidal suspension was subjected to a hydrothermal treatment at high temperature. The elevated temperature and pressure induce the transformation of the amorphous nanoparticles into highly crystalline primary particles. The proposed formation mechanism of the $IrB_{160\text{-}4}$ catalyst is consistent with the excessive-reductant-directed gelation strategy recently reported for noble metal sys-

tems [38]. A key driver in this process is the in situ generation of H_2 bubbles, which creates a significant disturbance in the reaction medium, thereby promoting effective collisions and the subsequent fusion of the iridium nanoparticles into uniform nanoclusters. This mechanism explains the accelerated growth and the high structural uniformity observed in our $IrB_{160\text{-}4}$ catalyst compared to conventional methods using low reductant-to-metal ratios.

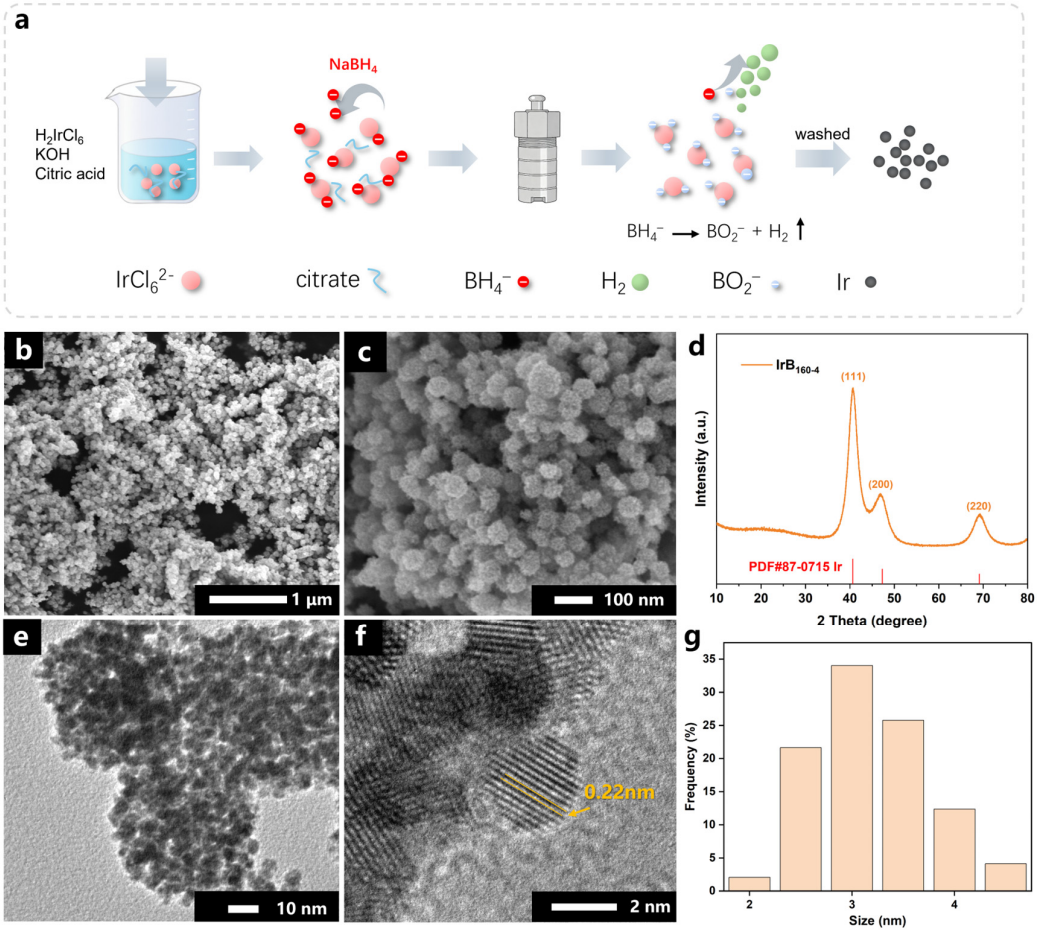

Figure 1. (**a**) Schematic illustration of the synthesis of $IrB_{160\text{-}4}$. (**b**,**c**) SEM, (**d**) XRD, (**e**,**f**) TEM and (**g**) particle size distribution of the $IrB_{160\text{-}4}$.

2.2. Systematic Optimization

To achieve an optimal balance between electrochemical activity and practical processability for industrial-scale manufacturing, the hydrothermal parameters were systematically investigated. Specifically, the dual effects of reaction temperature (100~160 °C) and duration (1~4 h) were evaluated, revealing that product properties are highly sensitive to these conditions.

As summarized in Table 1, lower temperatures or shorter reaction times (e.g., $IrB_{100\text{-}4}$ or $IrB_{160\text{-}1}$) consistently yielded turbid, gray colloidal solutions. These products were characterized by small particle sizes and low crystallinity, posing significant challenges for efficient separation via filtration and resulting in diminished yields. In stark contrast, the $IrB_{160\text{-}4}$ catalyst (160 °C for 4 h) yielded a clear supernatant and a well-precipitated black solid. This trend was confirmed by morphological characterization (Figures S1 and S2), which showed an evolution from amorphous aggregates to well-defined, more readily separable spherical particles with increasing temperature and time. This optimized product demonstrated excellent practical processability, allowing for rapid collection through simple filtration with a high recovery yield of 99%. The robust scalability of this one-pot aqueous

strategy is further exemplified by its high production efficiency; specifically, starting from 2.575 g of hexachloroiridic acid hexahydrate precursor, approximately 1 g of the $IrB_{160\text{-}4}$ catalyst powder can be consistently obtained in a single laboratory-scale batch. This indicates the potential for cost-effective, large-scale manufacturing with minimal precious metal loss.

Table 1. Effect of reaction temperature and time on the yield and properties of the obtained catalysts.

Catalyst	Temperature (°C)	Time (h)	Yield	Solution Appearance	Separation Method
$IrB_{160\text{-}1}$	160	1	94%	Turbid, grey	Filtration
$IrB_{160\text{-}2}$	160	2	98%	Clear and colorless	Filtration
$IrB_{160\text{-}4}$	160	4	99%	Clear and colorless	Filtration
$IrB_{130\text{-}4}$	130	4	93%	Clear and colorless	Filtration
$IrB_{100\text{-}4}$	100	4	77%	Turbid, grey	Centrifugation

Morphological evolution observed in Figures S1 and S2 confirms that increasing temperature and time promotes the transition from amorphous aggregates to well-defined, separable spherical particles. Crucially, Electrochemical activity tests (Figure 2) revealed that $IrB_{160\text{-}4}$ simultaneously exhibited the best catalytic activity. In summary, the 160 °C and 4 h condition ($IrB_{160\text{-}4}$) achieves the optimal balance between high catalytic activity and scalable, practical processability. Therefore, the optimized $IrB_{160\text{-}4}$ catalyst was selected for all subsequent performance evaluations.

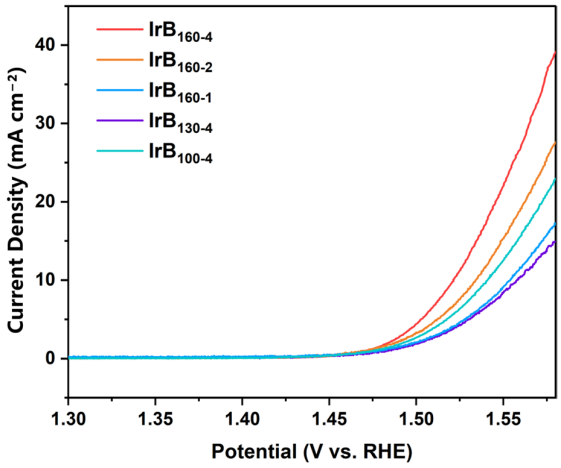

Figure 2. The linear sweep voltammograms of $IrB_{160\text{-}1}$, $IrB_{160\text{-}2}$, $IrB_{160\text{-}4}$, $IrB_{100\text{-}4}$ and $IrB_{130\text{-}4}$.

2.3. Structural Characterization of Catalysts

The textural properties of $IrB_{160\text{-}4}$ and commercial Ir-Black were investigated via N_2 adsorption–desorption measurements. As shown in Figure 3, the isotherms exhibit a visible hysteresis loop, indicating the presence of mesoporous structures. $IrB_{160\text{-}4}$ shows a higher nitrogen adsorption capacity than Ir-black, consistent with its larger BET surface area (60 m^2 g^{-1} vs. 48 m^2 g^{-1}). The pore size distribution curves reveal that $IrB_{160\text{-}4}$ possesses more pores in the 2–10 nm range. These pores likely correspond to the interstitial voids formed by the packing of the ~3 nm primary nanoparticles. This porosity facilitates electrolyte access to the active sites, contributing to the improved electrochemical performance.

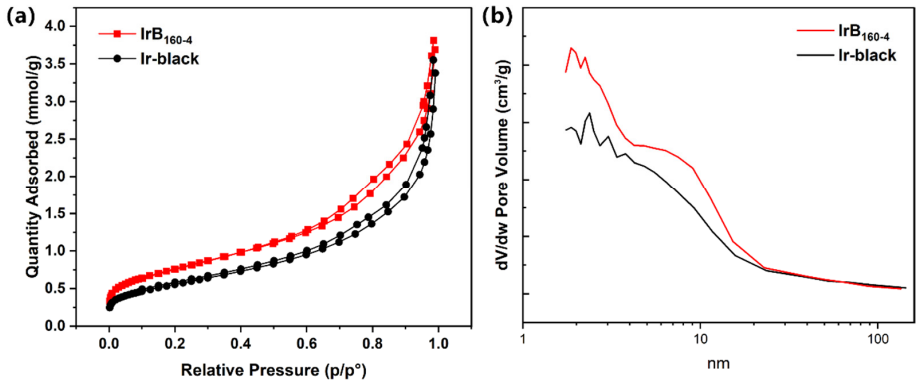

Figure 3. N_2 adsorption–desorption isotherms (**a**) and the corresponding pore size distribution curves (**b**) of $IrB_{160\text{-}4}$ and Ir-black.

Furthermore, XPS was employed to further probe the surface-specific chemical states and purity (as shown in Figure 4). The high-resolution Ir 4f spectrum reveals that the surface of $IrB_{160\text{-}4}$ consists of both metallic Ir^0 and oxidized Ir^{4+} species. This suggests that the $IrB_{160\text{-}4}$ catalyst features a surface-oxidized metallic structure, where a thin layer of IrO_2 covers the crystalline metallic core. Furthermore, the O 1s spectrum and the absence of significant impurity signals in XPS confirm the high purity of the catalyst, which is attributed to the thorough washing process and high-temperature hydrothermal crystallization. This unique structure maximizes the utilization of active sites through surface oxides while maintaining high overall conductivity through the metallic iridium framework, thus contributing to the excellent performance and durability in PEMWE.

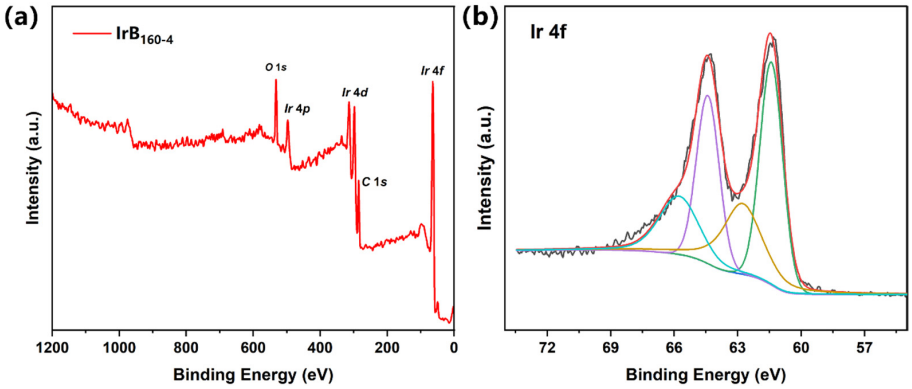

Figure 4. XPS spectra of the $IrB_{160\text{-}4}$: (**a**) survey spectrum and (**b**) high-resolution Ir 4f spectrum. In (**b**), the black line represents the raw data, and the red line is the fitted envelope. The deconvoluted peaks corresponding to metallic Ir^0 are shown in green and purple, while the peaks for oxidized Ir^{4+} species are shown in yellow and cyan.

2.4. Characterization of the Morphology of Catalysts

The morphology and microstructure of the optimized catalyst (named $IrB_{160\text{-}4}$) were characterized by scanning electron microscopy (SEM) images, as shown in Figure 1b,c. The $IrB_{160\text{-}4}$ exhibits uniformly distributed spherical particles over a wide area, indicating a high degree of structural homogeneity. The higher magnification image (Figure 1c) reveals that these spheres are agglomerates with an average diameter of approximately 50 nm. Such pronounced micrometer-scale uniformity can be attributed directly to the controlled synthesis process. Furthermore, this structure makes the nano catalyst powder easy to handle and can be separated from the reaction solution by simple filtration, demonstrating its potential for scalable production.

Furthermore, the structure of the catalyst was analyzed using transmission electron microscopy (TEM). As shown in Figure 1e, approximately 50 nm aggregates consist of a large number of nanoparticles. These primary nanoparticles exhibit a uniform, near-spherical morphology with a very small average particle size of ca. 3 ± 0.5 nm as shown in Figure 1g. The High-Resolution TEM image (Figure 1f) provides further insight into the nature of these primary nanoparticles. Clear and continuous lattice fringes are visible, demonstrating the high crystalline nature of the 3 nm nanoparticles. The measured lattice spacing of 0.22 nm corresponds well to the (111) plane of face-centered cubic Iridium.

The phase and crystal structure of the $IrB_{160\text{-}4}$ catalyst were also confirmed by X-ray Diffraction (XRD). As shown in Figure 1d, the diffraction peaks at 40.7°, 47.3°, and 69.1° are clearly observed, which are characteristic of the (111), (200) and (220) planes of Iridium [39–41]. These results demonstrate that $IrB_{160\text{-}4}$ features a structure where highly crystalline ~3 nm FCC Iridium primary nanoparticles are aggregated into 50 nm spherical particles. This unique structure is designed to maximize active site utilization while maintaining structural integrity.

2.5. Electrocatalytic Oxygen Evolution Reaction Activity

The electrocatalytic performance of $IrB_{160\text{-}4}$ catalyst for the OER was evaluated in a 0.5 M H_2SO_4 electrolyte using a standard three-electrode method. In addition, to compare the practical value of the as-prepared catalysts, commercial state-of-the-art Ir-Black were tested under identical conditions. Figure 5 displays the linear sweep voltammetry (LSV) polarization curves. The $IrB_{160\text{-}4}$ catalyst exhibits enhanced OER activity compared to the commercial Ir-Black catalyst. Notably, the $IrB_{160\text{-}4}$ catalyst requires an overpotential of only 291 mV (without iR-correction) to deliver a benchmark current density of 10 mA cm^{-2}, which is 18 mV lower than that required by Ir-Black catalyst (310 mV without iR-correction). To investigate the reaction kinetics, Tafel slopes were derived from the LSV curves. The $IrB_{160\text{-}4}$ shows a Tafel slope of 56 mV dec^{-1}, which is lower than that of Ir-Black (61 mV dec^{-1}). Based on a catalyst loading of 0.106 mg cm^{-2} on the glassy carbon electrode, the mass activity of $IrB_{160\text{-}4}$ at an overpotential of 291 mV was calculated to be 94.34 mA mg^{-1}_{Ir}. This is significantly higher than that of commercial Ir-Black (66.04 mA mg^{-1}_{Ir}). These results demonstrate that $IrB_{160\text{-}4}$ exhibits higher OER activity than the commercial Ir-Black. Table 2 shows the performance of $IrB_{160\text{-}4}$ with that of recently reported iridium-based catalysts for PEM water electrolysis. The comparison results clearly demonstrate that the $IrB_{160\text{-}4}$ catalyst exhibits high activity and durability compared to these materials. This superior performance can be attributed to its ultrasmall particle size and high size uniformity, which collectively lead to a greater utilization of active sites.

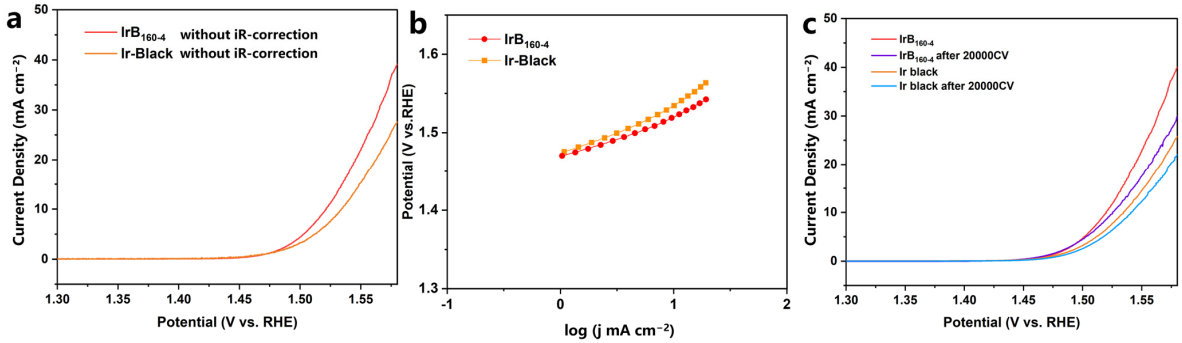

Figure 5. (**a**) LSV curves (without iR-correction), (**b**) Tafel plots of $IrB_{160\text{-}4}$ and commercial Ir-Black catalysts in 0.5 M H_2SO_4 (**c**) LSV curves of $IrB_{160\text{-}4}$ and commercial Ir black catalysts after 20,000 cycles.

Table 2. Summary of the performance of Ir-based electrocatalysts.

Anode Catalysts	Overpotential (mV) @10 mA/cm^2	Tafel Slope (mV/dec)	Ref.
IrO_2 nanoneedles	313	57	[42]
$IrO_x \cdot nH_2O$	300	47	[43]
IrO_x/Zr_2ON_2	255	48	[44]
Sr_2CaIrO_6	250	33	[45]
(La)IrO_x	256	57	[46]
Ir NS/TiO_2	~285	57.3	[47]
$IrB_{160\text{-}4}$	291	56	This work

To further evaluate the catalyst surface area under electrochemical conditions, the electrochemical double-layer capacitance (C_{dl}) was measured as shown in Figure 6. The C_{dl} of $IrB_{160\text{-}4}$ is 4.60 mF cm^{-2}, which is higher than that of commercial Ir-Black (2.95 mF cm^{-2}). Correspondingly, the calculated ECSA of $IrB_{160\text{-}4}$ is 123.9 m^2 g^{-1}, compared to 79.5 m^2 g^{-1} for Ir-Black. This high electrochemical surface availability is attributed to the hierarchical structure of the self-assembled $IrB_{160\text{-}4}$ nanospheres. Specifically, the ~50 nm nanoclusters, assembled from ~3 nm primary nanoparticles, help to mitigate the dense agglomeration typically observed in conventional iridium catalysts. As a result, $IrB_{160\text{-}4}$ maintains favorable electrolyte accessibility and wetting properties in the liquid phase, facilitating the exposure of active iridium sites during the oxygen evolution reaction. The hierarchical pores provide efficient mass transfer pathways and ensure high site utilization under operating conditions.

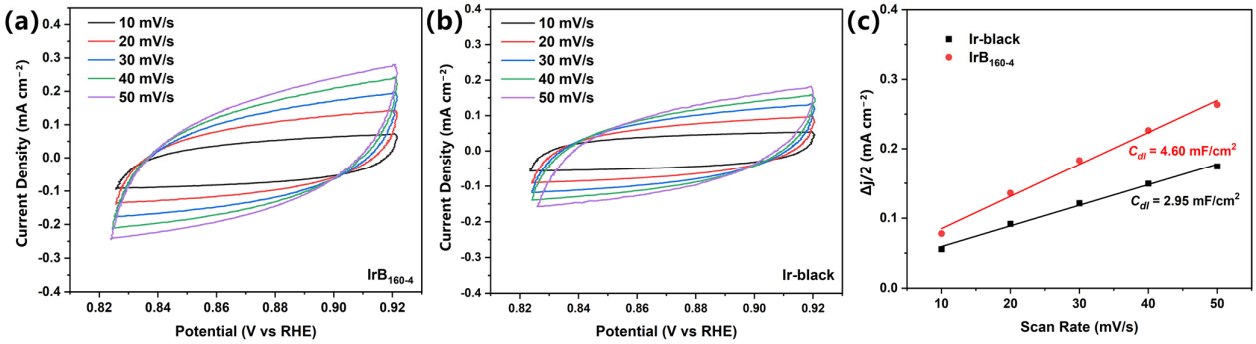

Figure 6. C_{dl} measurements for $IrB_{160\text{-}4}$ and Ir-black: (**a**,**b**) CV curves at different scan rates and (**c**) linear fitting of capacitive currents.

The durability of the catalysts was further evaluated through accelerated degradation testing, in which the electrode was subjected to continuous potential cycling. As illustrated in Figure 5c, the $IrB_{160\text{-}4}$ exhibits high electrochemical stability, showing a slight shift in only 8 mV at 10 mA cm^{-2} after 20,000 potential cycles. This relatively small loss of activity indicates that the structure and electronic properties of $IrB_{160\text{-}4}$ remain largely intact during long-term operation. Under the same test conditions, the voltage decay of the commercial Ir-Black catalyst is approximately 11 mV. These results confirm that $IrB_{160\text{-}4}$ has significantly enhanced durability, making it a promising anode catalyst candidate for long-term PEM water electrolysis applications.

2.6. PEMWE Performance

To evaluate the practical viability of the $IrB_{160\text{-}4}$ catalyst, it was integrated as the anode catalyst in a PEM single-cell MEA. The Ir loading of the anode catalyst was 0.5 mg cm^{-2},

while the cathode employed a Pt/C catalyst with a Pt loading of 0.5 mg cm^{-2}. A commercial Ir-Black based MEA was also fabricated and tested under identical conditions for comparison. The polarization curves of the single-cell MEAs operating at 80 °C are presented in Figure 7. The $IrB_{160\text{-}4}$ catalyst based MEA demonstrates superior performance across the entire current density range. Specifically, to achieve an industrial-scale current density of 2.0 A cm^{-2}, our MEA required a cell voltage of only 1.79 V, which is lower than the 1.81 V required by the Ir-Black MEA. This advantage becomes more pronounced at higher current densities, where our catalyst delivers 3.3 A cm^{-2} at only 2.0 V, indicative of improved reaction kinetics and more efficient mass transport under demanding operating conditions. This lower operating voltage directly translates to a significant improvement in the overall energy efficiency of the PEMWE system. To de-convolute the sources of this performance gain, Electrochemical Impedance Spectroscopy (EIS) was conducted at a constant cell voltage of 1.7 V. The resulting Nyquist plots are shown in Figure 3b. Both MEAs exhibit a similar high-frequency intercept, representing the ohmic resistance of the cell components. The $IrB_{160\text{-}4}$ MEAs exhibited significantly reduced high frequency resistance (159 mΩ cm^2) compared to the commercial Ir-Black MEA (167 mΩ cm^2). The charge-transfer resistance, represented by the semicircle diameter in the Nyquist plot, was significantly reduced for $IrB_{160\text{-}4}$ (20 mΩ cm^2) compared to Ir-Black (31 mΩ cm^2), indicating its enhanced OER kinetics.

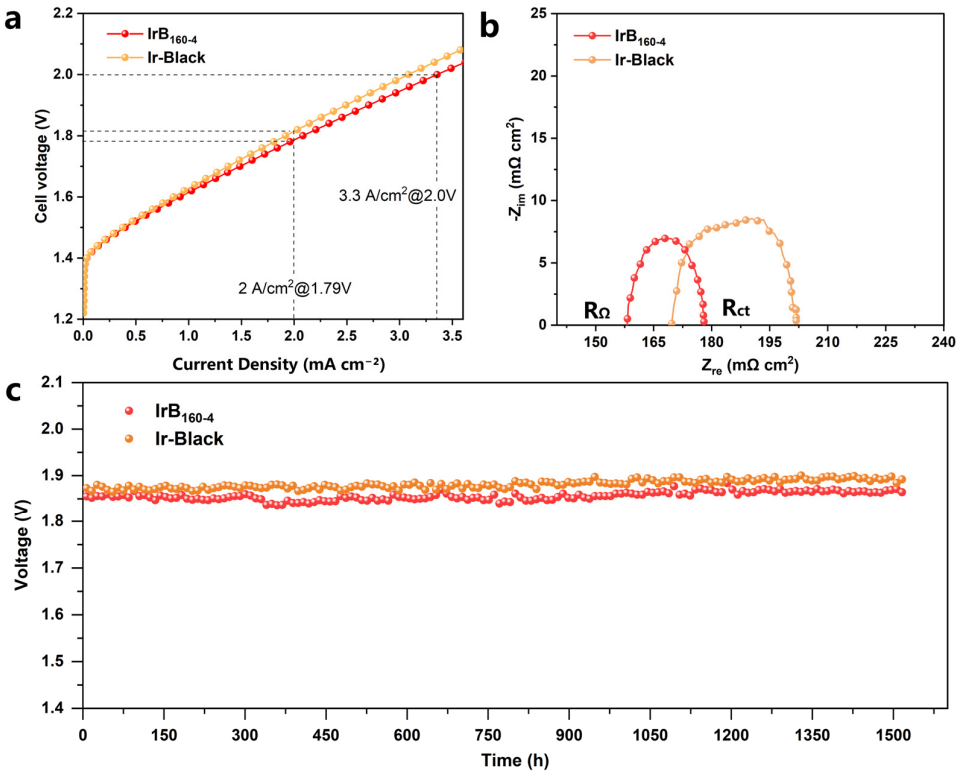

Figure 7. (**a**) The PEM water electrolysis performance at 80 °C and (**b**) EIS curves of the $IrB_{160\text{-}4}$ and commercial Ir-Black. (**c**) The stability test of $IrB_{160\text{-}4}$ and commercial Ir-Black at a current density of 2 A cm^{-2} at 60 °C.

To further assess the catalytic performance, we investigated the hydrogen evolution efficiency of the $IrB_{160\text{-}4}$-based MEA. The H_2 gas evolution rate was measured across a range of current densities via the water displacement method. As shown in Figure S3, the experimentally determined H_2 production rate (e.g., ~372 mL min^{-1} at 2.0 A cm^{-2}) closely matches the theoretical value derived from Faraday's law. This corresponds to a hydrogen

production efficiency of approximately 98%, underscoring the high catalytic efficiency of the $IrB_{160\text{-}4}$ catalyst for proton exchange membrane water electrolysis.

To assess the industrial potential of the $IrB_{160\text{-}4}$, we evaluated the Iridium (Ir) utilization efficiency, a key factor in the economics of PEMWE systems. Operating at a constant current of 2.0 A/cm^2 at 60 °C (1.85 V), the MEA with a loading of 0.5 mg_{Ir}/cm^2 achieves a specific Ir utilization of 0.169 g_{Ir}/kW_{H2} (based on 1.48 V HHV). This level of utilization represents a major step toward the cost-effective deployment of PEM electrolyzers. Furthermore, long-term durability tests conducted at 60 °C demonstrate its excellent stability and promising application potential.

The long-term operational stability, which represents a critical benchmark for the commercialization of PEMWE, was evaluated at 60 °C under a constant current density of 2.0 A cm^{-2}. The MEA incorporating the $IrB_{160\text{-}4}$ exhibited excellent stability, operating continuously for over 1500 h with a voltage degradation rate of 13 μV h^{-1}. In contrast, the MEA using commercial Ir-Black catalyst showed a degradation rate of 17 μV h^{-1} under the same conditions.

To further verify the structural robustness of the catalyst, post-mortem TEM characterization and particle size analysis were performed after the 1500 h durability test. As shown in Figure 8a, the $IrB_{160\text{-}4}$ catalyst maintained its original hierarchical morphology of spherical nanoclusters. Statistical analysis of the primary nanoparticles (Figure 8b) shows an average particle size of approximately 3.2 nm. Compared to the fresh catalyst (~3 nm), the distribution exhibits a subtle rightward shift, with most particles (over 80%) concentrated within the 2.5~4.0 nm range and the peak frequency centered at 3.0~3.5 nm. These results demonstrate that the excellent durability of $IrB_{160\text{-}4}$ stems from its stable structure and high crystallinity, which effectively suppresses the migration and aggregation of primary particles under the harsh high-potential operating conditions of PEMWE.

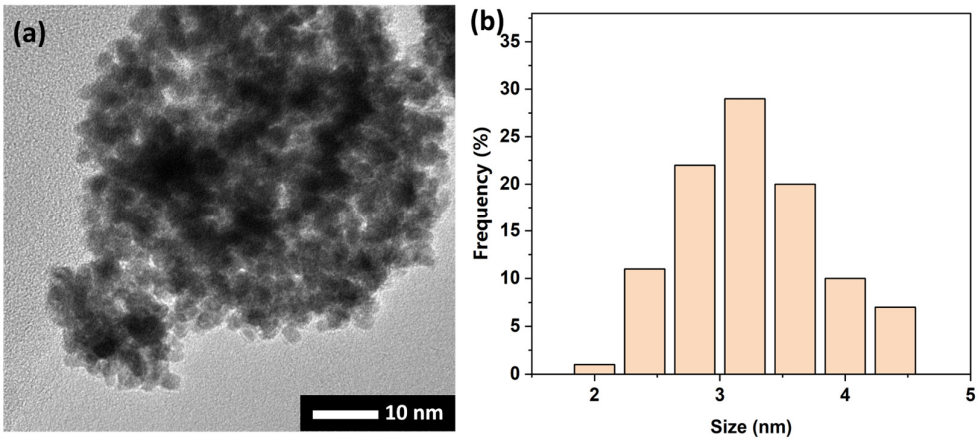

Figure 8. The (**a**) TEM and (**b**) particle size distribution of the $IrB_{160\text{-}4}$ after the stability test.

In addition, a comparison of the stability performance between our work and other state-of-the-art Ir-based catalysts reported in the recent literature is provided in Table 3. The $IrB_{160\text{-}4}$ catalyst shows a degradation rate of only 13 μV h^{-1} over 1500 h at a high current density of 2.0 A cm^{-2}. Compared to many doped IrO_X or structured iridium nanocatalysts, this catalyst demonstrates superior corrosion resistance. The superior durability of the $IrB_{160\text{-}4}$ is attributed to its high crystallinity and highly uniform, spherically self-assembled structure. This unique structure enhances the catalyst's corrosion resistance under highly acidic and high-potential operating conditions and effectively suppresses the migration and aggregation of primary particles, thereby ensuring its long-term operational stability.

Table 3. Recent iridium-based electrocatalysts and their performance in a single PEMWE.

Anode Catalysts	Membrane	Loading (mg/cm^2)	Stability (h)	Average Degradation Rate (μV/h)	Ref.
IrO_2 nanoneedles	Nafion 117	4	200 h@2 A/cm^2	-	[42]
IrO_2/TNO-H750	Nafion 117	2.5	100 h@1 A/cm^2	110	[48]
Ir/Nb_2O_{5-x}	Nafion 115	1.8	2000 h@2 A/cm^2	-	[49]
$IrO_x \cdot nH_2O$	Nafion 115	3.0	600 h@1 A/cm^2	5.9	[43]
Ir NS/TiO_2	Nafion 212	0.7	1000 h@1 A/cm^2	95	[47]
dh-IrO_x-230	Nafion 115	0.5	1000 h@2 A/cm^2 2000 h@1 A/cm^2	22/ 10	[50]
IrB_{160-4}	Nafion 115	0.5	1500 h@2 A/cm^2	13	This work

3. Materials and Method

3.1. Chemicals and Materials

Hexachloroiridic acid hexahydrate ($H_2IrCl_6 \cdot 6H_2O$, 99.9%), Citric acid (99.8%), Sodium borohydride ($NaBH_4$, 98%), were purchased from Aladdin Chemistry Co. Ltd. (Shanghai, China). Potassium hydroxide (KOH, ≥99.99%), Sulfuric acid (H_2SO_4, 98%), Isopropanol (IPA) were purchased from Macklin Biochemical Co. Ltd., (Shanghai, China). All chemicals were used as received. Commercial Iridium Black (Ir-Black) and Pt/C (40 wt% Pt, Johnson Matthey, London, UK) were used as commercial benchmark catalysts. Nafion D520 solution (5 wt%) and Nafion 115 membranes were purchased from Chemours. All experiments used high-purity deionized water (DI water, 18.2 MΩ·cm).

3.2. Synthesis of Catalysts IrBx

Taking the synthesis of IrB_{160-4} as an example, 2.575 g of hexachloroiridic acid hexahydrate and 0.96 g of citric acid were added to a 500 mL beaker. Subsequently, 250 mL of DI water was added, and the mixture was dissolved under vigorous stirring for 20 min to form a homogeneous precursor solution. Then 1.4 g of KOH was dissolved in 40 mL of DI water to prepare a KOH solution. This solution was then added dropwise to the above solution at room temperature. After the addition was complete, the mixture was stirred for an additional 30 min. Next, 1.9 g of $NaBH_4$ was dissolved in 60 mL of DI water to prepare a fresh reducing solution. This freshly prepared $NaBH_4$ solution was added dropwise at a slow rate (1 drop every 1–2 s) into the vigorously stirred mixture solution. The solution was then left to stir for another 30 min. The resulting mixture was subsequently transferred into a Teflon-lined stainless-steel autoclave and heated at 160 °C for 4 h. After the reaction, the autoclave was allowed to cool naturally to room temperature. The product was collected, revealing a clear supernatant and a black precipitate. The precipitate was separated by filtration and washed several times with ample DI water to remove residual impurities. Finally, the solid product was dried in an oven at 60 °C for 8 h. The dried product was ground into a fine powder to obtain the final catalyst.

The other catalysts were synthesized using an identical procedure, only varying the reaction temperature and duration. Specifically, IrB_{160-1} (160 °C, 1 h), IrB_{160-2} (160 °C, 2 h), IrB_{100-4} (100 °C, 4 h), and IrB_{130-4} (130 °C, 4 h) were prepared by adjusting these two parameters accordingly.

3.3. Physical Characterization

The crystallographic structure of the as-prepared catalyst was analyzed by X-ray diffraction (XRD) using a Bruker D8 Advance diffractometer (Bruker, Karlsruhe, Germany) equipped with a Cu Kα radiation source (λ = 1.5418 Å) at 40 kV and 40 mA. The surface

chemical compositions and valence states were analyzed by X-ray photoelectron spectroscopy (XPS, Thermo Scientific K-Alpha, Thermo Fisher Scientific, Waltham, MA, USA), with all binding energies calibrated to the C 1s peak at 284.8 eV. The specific surface area of the catalyst was determined using the N_2 adsorption–desorption isotherm via a Micromeritics ASAP 2460 system (Micromeritics, Norcross, GA, USA). The surface morphology was examined using a field-emission scanning electron microscope (SEM, JEOL 7800F, JEOL Ltd., Tokyo, Japan) at an accelerating voltage of 15 kV. Further investigation of the catalyst's nanostructure and lattice fringes was conducted via transmission electron microscopy (TEM) on a JEOL JEM-2100F microscope (JEOL Ltd., Tokyo, Japan) operating at 200 kV. Samples for electron microscopy were prepared by depositing a drop of ultrasonically dispersed ethanol suspension onto a carbon-coated copper grid.

3.4. Electrochemical Measurements

All electrochemical evaluations were performed at room temperature (~25 °C) using an AutoLab PGSTAT302N electrochemical workstation (Metrohm Autolab, Utrecht, The Netherlands) in a standard three-electrode configuration. The electrolyte was a 0.5 M H_2SO_4 aqueous solution. To prepare the working electrode, a catalyst ink was formulated by dispersing 5 mg of catalyst powder in a solution containing 1.8 mL of isopropanol, 1.8 mL of deionized water, and 50 μL of Nafion solution (5 wt%). The mixture was ultrasonicated for 60 min to ensure a homogeneous suspension. A 5 μL aliquot of the ink was then drop-casted onto a polished glassy carbon electrode (GCE, 5 mm diameter). Specifically, to ensure a uniform catalyst layer, the 5 μL of catalyst ink was dropped onto the GCE three times. Based on the ink concentration, the total mass of catalyst on the electrode was approximately 20.55 μg, with a mass loading of 0.106 mg/cm^2. A saturated calomel electrode (SCE) and a platinum (Pt) wire served as the reference and counter electrodes, respectively. All potentials were converted to the reversible hydrogen electrode (RHE) scale using the equation: E (vs. RHE) = E (vs. SCE) + 0.241 V + 0.0591 × pH. All catalysts were activated by 50 cycles of cyclic voltammetry at a scan rate of 100 mV s^{-1} in an N_2-saturated electrolyte before electrochemical tests. Linear sweep voltammetry was conducted in the potential range of 1.2 to 1.6 V vs. RHE at a scan rate of 5 mV s^{-1} to record the oxygen evolution reaction polarization curves. All polarization curves and overpotential values in the three-electrode tests are reported without iR-correction to reflect the raw experimental data. The stability of the catalyst was evaluated by performing cyclic voltammetry for 20,000 cycles at a scan rate of 100 mV s^{-1}. The electrochemically active surface area (ECSA) was estimated from the double-layer capacitance (C_{dl}) via the equation: ECSA = $C_{dl}/(C_s \times m)$, where m is the catalyst mass loading and Cs is the specific capacitance of a flat surface (0.035 mF cm^{-2}). Subsequently, the LSV test was repeated to assess the electrocatalytic performance.

3.5. Membrane Electrode Assembly Fabrication

The synthesized catalyst and a commercial Pt/C (40 wt%) catalyst were used for the anode and cathode, respectively. The anode catalyst ink was prepared by ultrasonically dispersing the IrB_x powder in a mixture of Nafion D520 and an isopropanol/water (2:1) solvent for 2 h. The ink was then sprayed directly onto a Nafion 115 proton exchange membrane using an automated spray-coater to form a catalyst-coated membrane (CCM). The effective active area of the MEA was 25 cm^2. The anode iridium loading was controlled at 0.5 mg cm^{-2}. Subsequently, the cathode ink was sprayed onto the opposite side of the membrane to achieve a platinum loading of 0.5 mg cm^{-2}. The fabricated CCM was dried in a vacuum oven at 80 °C for 2 h prior to cell assembly. Finally, the membrane electrode was

hot-pressed at 10 MPa and 120 °C for 5 min to ensure a closer bond between the catalyst and the membrane.

3.6. MEA Single-Cell Testing

The MEA was assembled into a single cell with an active area of 25 cm^2, with a deionized water flow rate of 100 $mL \cdot min^{-1}$. Titanium felt (0.25 mm, with 2 μm Pt coating) and carbon paper (0.18 mm) were used as the gas diffusion layers for the anode and cathode, respectively. Prior to testing, the MEA underwent a constant current test at 1 $A \cdot cm^{-2}$ for 24 h. Finally, polarization curves were recorded by performing voltage scans from 1.3 to 2.1 V at a scan rate of 10 $mV \cdot s^{-1}$. To determine the high-frequency resistance, electrochemical impedance spectroscopy was conducted at 1.9 V, with a frequency range of 10 kHz to 1 Hz and an amplitude of 15 mV. The HFR was obtained from the high-frequency intercept on the real axis of the Nyquist plot. A long-term durability test was performed at a constant current density of 2.0 A cm^{-2} at 60 °C for 1500 h.

4. Conclusions

In summary, this work reports a simple, scalable, and environmentally friendly one-pot aqueous synthesis of a high-performance Ir-based OER catalyst composed of large-scale uniform spherical nanoclusters. These nanoclusters are self-assembled from highly crystalline ~3 nm Ir nanoparticles, a structure that facilitates straightforward product filtration and scalable processing. Performance evaluations demonstrated that the catalyst exhibits OER activity superior to that of commercial Ir-Black. More importantly, when integrated into an MEA, the catalyst achieved a low operating voltage of 1.79 V at a high current density of 2.0 A cm^{-2} and maintained excellent long-term durability for over 1500 h with a minimal degradation rate of 13 μV h^{-1}. This superior overall performance can be attributed to its high crystallinity and uniform self-assembled structure, which enhances both intrinsic activity and corrosion resistance. This work not only provides a highly efficient OER catalyst but also proposes a practical and scalable synthesis strategy, offering a viable pathway for the development of industrial-grade, high-performance, and cost-effective anode catalysts for PEM water electrolysis.

Supplementary Materials: The following supporting information can be downloaded at https://www.mdpi.com/article/10.3390/catal16050430/s1, Figure S1: SEM of the (a) $IrB_{160\text{-}1}$ (b) $IrB_{160\text{-}2}$ (c) $IrB_{160\text{-}4}$ (d) $IrB_{100\text{-}4}$ (e) $IrB_{130\text{-}4}$; Figure S2: TEM of the (a) $IrB_{160\text{-}1}$ (b) $IrB_{160\text{-}2}$ (c) $IrB_{100\text{-}4}$ (d) $IrB_{130\text{-}4}$; Figure S3: The H_2 production at different current densities.

Author Contributions: Conceptualization, C.L., Y.A. and Y.W.; methodology and investigation, C.L., Y.A., B.X., F.F., J.W. and C.S.; writing, C.L. and Y.A.; supervision and funding acquisition, H.X., Y.Y. and Y.W. All authors have read and agreed to the published version of the manuscript.

Funding: This research was funded by Petrochina Science and Technology Management Department, grant numbers 2021-CB-11-05, 2022DJ5006(GF), LH-2025-43 and 2024DQ03193.

Data Availability Statement: Data is contained within the article and Supplementary Materials.

Conflicts of Interest: There are no conflicts to declare.

References

1. Araújo, H.F.; Gómez, J.A.; Santos, D.M.F. Proton-Exchange Membrane Electrolysis for Green Hydrogen Production: Fundamentals, Cost Breakdown, and Strategies to Minimize Platinum-Group Metal Content in Hydrogen Evolution Reaction Electrocatalysts. *Catalysts* **2024**, *14*, 845. [CrossRef]
2. Suen, N.-T.; Hung, S.-F.; Quan, Q.; Zhang, N.; Xu, Y.-J.; Chen, H.M. Electrocatalysis for the Oxygen Evolution Reaction: Recent Development and Future Perspectives. *Chem. Soc. Rev.* **2017**, *46*, 337–365. [CrossRef] [PubMed]

3. Hassan, N.S.; Jalil, A.A.; Rajendran, S.; Khusnun, N.F.; Bahari, M.B.; Johari, A.; Kamaruddin, M.J.; Ismail, M. Recent Review and Evaluation of Green Hydrogen Production via Water Electrolysis for a Sustainable and Clean Energy Society. *Int. J. Hydrogen Energy* **2024**, *52*, 420–441. [CrossRef]
4. Xia, Y.; Rajappan, S.C.; Kraglund, M.R.; Serhiichuk, D.; Pan, D.; Chen, S.; Jensen, J.O.; Jannasch, P.; Aili, D. Tetrazole-Functionalized Poly(Oxindole Biphenylene) Ion-Solvating Membranes for Alkaline Water Electrolysis. *J. Power Sources* **2025**, *656*, 238047. [CrossRef]
5. Yan, D.; Mebrahtu, C.; Wang, S.; Palkovits, R.; Liu, Z.; Lan, J.; Xia, X.; Ren, T.; Wang, X.; Guo, R.; et al. Low-Cost Flexible Textile Electrocatalyst for Overall Water Splitting. *Chem. Commun.* **2023**, *59*, 13883–13886. [CrossRef] [PubMed]
6. Yan, D.; Mebrahtu, C.; Wang, S.; Palkovits, R. Innovative Electrochemical Strategies for Hydrogen Production: From Electricity Input to Electricity Output. *Angew. Chem.-Int. Ed.* **2023**, *62*, e202214333. [CrossRef]
7. Liu, R.-T.; Xu, Z.-L.; Li, F.-M.; Chen, F.-Y.; Yu, J.-Y.; Yan, Y.; Chen, Y.; Xia, B.Y. Recent Advances in Proton Exchange Membrane Water Electrolysis. *Chem. Soc. Rev.* **2023**, *52*, 5652–5683. [CrossRef]
8. Tran, D.T.; Tran, P.K.L.; Malhotra, D.; Nguyen, T.H.; Nguyen, T.T.A.; Duong, N.T.A.; Kim, N.H.; Lee, J.H. Current Status of Developed Electrocatalysts for Water Splitting Technologies: From Experimental to Industrial Perspective. *Nano Converg.* **2025**, *12*, 9. [CrossRef]
9. Tao, H.B.; Liu, H.; Lao, K.; Pan, Y.; Tao, Y.; Wen, L.; Zheng, N. The Gap between Academic Research on Proton Exchange Membrane Water Electrolysers and Industrial Demands. *Nat. Nanotechnol.* **2024**, *19*, 1074–1076. [CrossRef]
10. Ede, S.R.; Luo, Z. Tuning the Intrinsic Catalytic Activities of Oxygen-Evolution Catalysts by Doping: A Comprehensive Review. *J. Mater. Chem. A* **2021**, *9*, 20131–20163. [CrossRef]
11. Thao, N.T.T.; Jang, J.U.; Nayak, A.K.; Han, H. Current Trends of Iridium-Based Catalysts for Oxygen Evolution Reaction in Acidic Water Electrolysis. *Small Sci.* **2024**, *4*, 2300109. [CrossRef] [PubMed]
12. Lin, B.-L.; Chen, X.; Niu, B.-T.; Lin, Y.-T.; Chen, Y.-X.; Lin, X.-M. The Research Progress of Ruthenium-Based Catalysts for the Alkaline Hydrogen Evolution Reaction in Water Electrolysis. *Catalysts* **2024**, *14*, 671. [CrossRef]
13. Sun, X.; Xu, K.; Fleischer, C.; Liu, X.; Grandcolas, M.; Strandbakke, R.; Bjørheim, T.S.; Norby, T.; Chatzitakis, A. Earth-Abundant Electrocatalysts in Proton Exchange Membrane Electrolyzers. *J. Membr. Sci.* **2024**, *8*, 657. [CrossRef]
14. Pang, B.; Feng, S.; Xu, Y.; Chen, H.; Li, J.; Yuan, Y.; Zou, X.; Tian, X.; Kang, Z. Ru Doped Ir Nanowires for High-Efficient and Durable Proton Exchange Membrane Water Electrolyzers. *Adv. Funct. Mater.* **2024**, *34*, 2411062. [CrossRef]
15. Yue, Y.; Zhu, K.; Li, X.; Ye, K. Porous Metal-Based Catalysts for Water Electrolysis. *Mater. Futures* **2025**, *4*, 032001. [CrossRef]
16. Kong, S.; Li, A.; Long, J.; Adachi, K.; Hashizume, D.; Jiang, Q.; Fushimi, K.; Ooka, H.; Xiao, J.; Nakamura, R. Acid-Stable Manganese Oxides for Proton Exchange Membrane Water Electrolysis. *Nat. Catal.* **2024**, *7*, 252–261. [CrossRef]
17. Shi, W.; Shen, T.; Xing, C.; Sun, K.; Yan, Q.; Niu, W.; Yang, X.; Li, J.; Wei, C.; Wang, R.; et al. Ultrastable Supported Oxygen Evolution Electrocatalyst Formed by Ripening-Induced Embedding. *Science* **2025**, *387*, 791–796. [CrossRef]
18. Chen, F.-Y.; Qiu, C.; Wu, Z.-Y.; Wi, T.-U.; Finfrock, Y.Z.; Wang, H. Ruthenium-Lead Oxide for Acidic Oxygen Evolution Reaction in Proton Exchange Membrane Water Electrolysis. *Nano Res.* **2024**, *17*, 8671–8677. [CrossRef]
19. Li, Y.; Dou, Z.; Pan, Y.; Zhao, H.; Yao, L.; Wang, Q.; Zhang, C.; Yue, Z.; Zou, Z.; Cheng, Q.; et al. Crystalline Phase Engineering to Modulate the Interfacial Interaction of the Ruthenium/Molybdenum Carbide for Acidic Hydrogen Evolution. *Nano Lett.* **2024**, *24*, 5705–5713. [CrossRef] [PubMed]
20. Zheng, W.-X.; Cheng, X.-X.; Chen, P.-P.; Wang, L.-L.; Duan, Y.; Feng, G.-J.; Wang, X.-R.; Li, J.-J.; Zhang, C.; Yu, Z.-Y.; et al. Boosting the Durability of RuO_2 via Confinement Effect for Proton Exchange Membrane Water Electrolyzer. *Nat. Commun.* **2025**, *16*, 337. [CrossRef] [PubMed]
21. Venkatesan, S.; Mitzel, J.; Ambu, S.S.; Morawietz, T.; Biswas, I.; Recalde, O.; Adabifiroozjaei, E.; Molina-Luna, L.; Estes, D.P.; Wegner, K.; et al. Rapid Scalable One-step Production of Catalysts for Low-Iridium Content Proton Exchange Membrane Water Electrolyzers. *Adv. Energy Mater.* **2025**, *15*, 2401659. [CrossRef]
22. Wang, C.; Guo, W.; Chen, T.; Lu, W.; Song, Z.; Yan, C.; Feng, Y.; Gao, F.; Zhang, X.; Rao, Y.; et al. Advanced Noble-Metal/Transition-Metal/Metal-Free Electrocatalysts for Hydrogen Evolution Reaction in Water-Electrolysis for Hydrogen Production. *Coord. Chem. Rev.* **2024**, *514*, 215899. [CrossRef]
23. Qin, R.; Chen, G.; Feng, X.; Weng, J.; Han, Y. Ru/Ir-Based Electrocatalysts for Oxygen Evolution Reaction in Acidic Conditions: From Mechanisms, Optimizations to Challenges. *Adv. Sci.* **2024**, *11*, 2309364. [CrossRef]
24. Zhang, M.; An, W.; Liu, Q.; Jiang, Y.; Zhao, X.; Chen, H.; Zou, Y.; Liang, X.; Zou, X. Tunnel-Structured IrO_x Unlocks Catalytic Efficiency in Proton Exchange Membrane Water Electrolyzers. *Nat. Commun.* **2025**, *16*, 7608. [CrossRef] [PubMed]
25. Zhang, J.; Fu, X.; Kwon, S.; Chen, K.; Liu, X.; Yang, J.; Sun, H.; Wang, Y.; Uchiyama, T.; Uchimoto, Y.; et al. Tantalum-Stabilized Ruthenium Oxide Electrocatalysts for Industrial Water Electrolysis. *Science* **2025**, *387*, 48–55. [CrossRef]
26. Wallnöfer-Ogris, E.; Grimmer, I.; Ranz, M.; Höglinger, M.; Kartusch, S.; Rauh, J.; Macherhammer, M.-G.; Grabner, B.; Trattner, A. A Review on Understanding and Identifying Degradation Mechanisms in PEM Water Electrolysis Cells: Insights for Stack Application, Development, and Research. *Int. J. Hydrogen Energy* **2024**, *65*, 381–397. [CrossRef]

27. Wang, S.; Lu, A.; Zhong, C.-J. Hydrogen Production from Water Electrolysis: Role of Catalysts. *Nano Converg.* **2021**, *8*, 4. [CrossRef] [PubMed]
28. Spöri, C.; Kwan, J.T.H.; Bonakdarpour, A.; Wilkinson, D.P.; Strasser, P. The Stability Challenges of Oxygen Evolving Catalysts: Towards a Common Fundamental Understanding and Mitigation of Catalyst Degradation. *Angew. Chem. Int. Ed.* **2017**, *56*, 5994–6021. [CrossRef] [PubMed]
29. Wang, Y.; Yan, H.; Fu, H. Recent Advances and Modulation Tactics in Ru- and Ir-Based Electrocatalysts for PEMWE Anodes at Large Current Densities. *eScience* **2025**, *5*, 100323. [CrossRef]
30. Quinson, J. Iridium and IrO_x Nanoparticles: An Overview and Review of Syntheses and Applications. *Adv. Colloid Interface Sci.* **2022**, *303*, 102643. [CrossRef]
31. Liao, F.; Yin, K.; Ji, Y.; Zhu, W.; Fan, Z.; Li, Y.; Zhong, J.; Shao, M.; Kang, Z.; Shao, Q. Iridium Oxide Nanoribbons with Metastable Monoclinic Phase for Highly Efficient Electrocatalytic Oxygen Evolution. *Nat. Commun.* **2023**, *14*, 1248. [CrossRef]
32. Zhu, J.; Elnabawy, A.O.; Lyu, Z.; Xie, M.; Murray, E.A.; Chen, Z.; Jin, W.; Mavrikakis, M.; Xia, Y. Facet-Controlled Pt–Ir Nanocrystals with Substantially Enhanced Activity and Durability towards Oxygen Reduction. *Mater. Today* **2020**, *35*, 69–77. [CrossRef]
33. Sonawane, J.R.; Jundale, R.; Kulkarni, A.A. Continuous Flow Synthesis of Metal Nanowires: Protocols, Engineering Aspects of Scale-up and Applications. *Mater. Horiz.* **2025**, *12*, 364–400. [CrossRef]
34. Kim, J.; Kwon, T.; Lee, J.; Lee, H.J.; Jun, M.; Ham, H.C.; Ju, H.; Kim, S.; Kim, J.Y. Ultrahigh Electrode Performance of Low-Loaded Iridium Jagged Nanotubes for Water Electrolysis Applications. *Adv. Energy Mater.* **2024**, *14*, 2400999. [CrossRef]
35. Yao, L.; Zhang, F.; Yang, S.; Zhang, H.; Li, Y.; Yang, C.; Yang, H.; Cheng, Q. Sub-2 Nm IrRuNiMoCo High-Entropy Alloy with Iridium-Rich Medium-Entropy Oxide Shell to Boost Acidic Oxygen Evolution. *Adv. Mater.* **2024**, *36*, 2314049. [CrossRef] [PubMed]
36. Tao, L.; Lv, F.; Wang, D.; Luo, H.; Lin, F.; Gong, H.; Mi, H.; Wang, S.; Zhang, Q.; Gu, L.; et al. Mass-Efficient Catalyst Layer of Hierarchical Sub-Nanosheets on Nanowire for Practical Proton Exchange Membrane Electrolyzer. *Joule* **2024**, *8*, 450–460. [CrossRef]
37. Lyu, X.; Chang, H.-M.; Yu, H.; Kariuki, N.N.; Park, J.H.; Myers, D.J.; Yang, J.; Zenyuk, I.V.; Serov, A. Evaluation of IrO_2 Catalysts Doped with Ti and Nb at Industrially Relevant Electrolyzer Conditions: A Comprehensive Study. *Chem. Eng. J.* **2025**, *505*, 159317. [CrossRef]
38. Du, R.; Wang, J.; Wang, Y.; Hübner, R.; Fan, X.; Senkovska, I.; Hu, Y.; Kaskel, S.; Eychmüller, A. Unveiling Reductant Chemistry in Fabricating Noble Metal Aerogels for Superior Oxygen Evolution and Ethanol Oxidation. *Nat. Commun.* **2020**, *11*, 1590. [CrossRef] [PubMed]
39. Xu, Y.; Wang, Y.; Qian, J.; Cai, D.; Nie, H.; Zhou, X.; Yang, Z. Ultrasmall Iridium Nanoparticles on Nitrogen-Doped Carbon Cloth for Efficient and Durable Acidic Water Splitting. *Chem. Commun.* **2025**, *61*, 16022–16025. [CrossRef]
40. Wang, J.; Ni, M.; Qian, J.; Ge, Y.; Cai, D.; Nie, H.; Zhou, X.; Yang, Z. Ultrafine Ir Nanoparticles Anchored on Carbon Nanotubes as Efficient Bifunctional Oxygen Catalysts for Zn–Air Batteries. *Chem. Commun.* **2024**, *60*, 6415–6418. [CrossRef]
41. Wang, Q.; Xu, C.-Q.; Liu, W.; Hung, S.-F.; Bin Yang, H.; Gao, J.; Cai, W.; Chen, H.M.; Li, J.; Liu, B. Coordination Engineering of Iridium Nanocluster Bifunctional Electrocatalyst for Highly Efficient and pH-Universal Overall Water Splitting. *Nat. Commun.* **2020**, *11*, 4246. [CrossRef]
42. Lim, J.; Park, D.; Jeon, S.S.; Roh, C.; Choi, J.; Yoon, D.; Park, M.; Jung, H.; Lee, H. Ultrathin IrO_2 Nanoneedles for Electrochemical Water Oxidation. *Adv. Funct. Mater.* **2018**, *28*, 1704796. [CrossRef]
43. Xu, J.; Jin, H.; Lu, T.; Li, J.; Liu, Y.; Davey, K.; Zheng, Y.; Qiao, S.-Z. $IrO_x{\cdot}nH_2O$ with Lattice Water–Assisted Oxygen Exchange for High-Performance Proton Exchange Membrane Water Electrolyzers. *Sci. Adv.* **2023**, *9*, eadh1718. [CrossRef]
44. Lee, C.; Shin, K.; Park, Y.; Yun, Y.H.; Doo, G.; Jung, G.H.; Kim, M.; Cho, W.; Kim, C.; Lee, H.M.; et al. Catalyst-support Interactions in Zr_2ON_2 -supported IrO_x Electrocatalysts to Break the Trade-off Relationship between the Activity and Stability in the Acidic Oxygen Evolution Reaction. *Adv. Funct. Mater.* **2023**, *33*, 2301557. [CrossRef]
45. Wang, Y.; Zhang, M.; Kang, Z.; Shi, L.; Shen, Y.; Tian, B.; Zou, Y.; Chen, H.; Zou, X. Nano-Metal Diborides-Supported Anode Catalyst with Strongly Coupled TaO_x/IrO_2 Catalytic Layer for Low-Iridium-Loading Proton Exchange Membrane Electrolyzer. *Nat. Commun.* **2023**, *14*, 5119. [CrossRef] [PubMed]
46. Wang, D.; Luo, H.; Lin, F.; Cao, S.; Wang, Y.; Zhang, D.; He, N.; Li, L.; Wang, Y.; Zhang, B.; et al. Local Hollandite Phase Inducing Oxygen Path Mechanism Enables Durable PEM Electrolysis. *Adv. Mater.* **2026**, e21163. [CrossRef]
47. Shin, D.; Lee, S.J.; Bak, J.; Roh, J.; Lee, K.; Chang, H.; Lee, H.; Kim, M.; Yang, H.J.; Kim, S.; et al. Ultrathin Iridium Nanosheets on Titanium Oxide for High-Efficiency and Durable Proton Exchange Membrane Water Electrolysis. *ACS Nano* **2025**, *19*, 42556–42565. [CrossRef]
48. Lv, H.; Wang, S.; Hao, C.; Zhou, W.; Li, J.; Xue, M.; Zhang, C. Oxygen-deficient $Ti_{0.9}Nb_{0.1}O_{2-x}$ as an Efficient Anodic Catalyst Support for PEM Water Electrolyzer. *ChemCatChem* **2019**, *11*, 2511–2519. [CrossRef]

49. Shi, Z.; Li, J.; Jiang, J.; Wang, Y.; Wang, X.; Li, Y.; Yang, L.; Chu, Y.; Bai, J.; Yang, J.; et al. Enhanced Acidic Water Oxidation by Dynamic Migration of Oxygen Species at the Ir/Nb_2O_{5-x} Catalyst/Support Interfaces. *Angew. Chem. Int. Ed.* **2022**, *61*, e202212341. [CrossRef] [PubMed]
50. Sun, K.; Liang, X.; Wang, X.; Wu, Y.A.; Jana, S.; Zou, Y.; Zhao, X.; Chen, H.; Zou, X. Highly Efficient and Durable Anode Catalyst Layer Constructed with Deformable Hollow IrO_x Nanospheres in Low-iridium PEM Water Electrolyzer. *Angew. Chem. Int. Ed.* **2025**, *137*, e202504531. [CrossRef]